JOURNAL OF THE AMERICAN CHEMICAL SOCIETY
pubs.acs.org/JACS
Article

Dynamic Nanocrystal Superlattices with Thermally Triggerable Lubricating Ligands

Yifan Ning,[#] Shengsong Yang,[#] Dai-Bei Yang,[#] Yi-Yu Cai, Jun Xu, Ruipeng Li, Yugang Zhang, Cherie R. Kagan, Jeffery G. Saven,[*] and Christopher B. Murray[*]

Cite This: J. Am. Chem. Soc. 2024, 146, 3785−3795
Read Online

ACCESS | Metrics & More | Article Recommendations | Supporting Information

ABSTRACT: The size-dependent and collective physical properties of nanocrystals (NCs) and their self-assembled superlattices (SLs) enable the study of mesoscale phenomena and the design of metamaterials for a broad range of applications. However, the limited mobility of NC building blocks in dried NCSLs often hampers the potential for employing postdeposition methods to produce high-quality NCSLs. In this study, we present tailored promesogenic ligands that exhibit a lubricating property akin to thermotropic liquid crystals. The lubricating ability of ligands is thermally triggerable, allowing the dry solid NC aggregates deposited on the substrates with poor ordering to be transformed into NCSLs with high crystallinity and preferred orientations. The interplay between the dynamic behavior of NCSLs and the molecular structure of the ligands is elucidated through a comprehensive analysis of their lubricating efficacy using both experimental and simulation approaches. Coarse-grained molecular dynamic modeling suggests that a shielding layer from mesogens prevents the interdigitation of ligand tails, facilitating the sliding between outer shells and consequently enhancing the mobility of NC building blocks. The dynamic organization of NCSLs can also be triggered with high spatial resolution by laser illumination. The principles, kinetics, and utility of lubricating ligands could be generalized to unlock stimuli-responsive metamaterials from NCSLs and contribute to the fabrication of NCSLs.

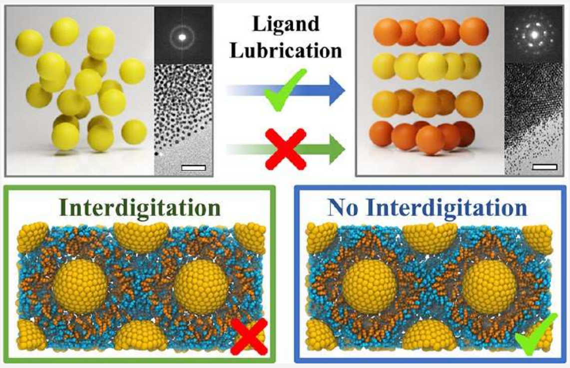

INTRODUCTION

The applications of nanocrystals (NCs) in optical devices,[1] catalysis,[2] and sensors[3] rely on the organization of NCs,[4,5] which can be achieved through the self-assembly of NCs into superlattices (SLs).[6,7] A persistent issue hindering the manufacturing of NCSLs is the lack of mobility of NC building blocks once the NCSLs are formed as dry solids.[8] Researchers attempted to address this issue by incorporating the NCs in a polymer matrix or with extended ligands,[9−12] and the versatility of these organic−inorganic hybrid materials showed the excellent potential of NCSLs as smart materials.[13,14] However, in most former cases, the volume fractions of NC cores in the assemblies were relatively low, typically 10% or less,[8,15] and the dynamics mainly arise from the organics serving as a flux or matrix to carry the NCs[15,16] and determine the final structure.

The low mobility of NCs not only hampers the ability to enhance the NCSL crystallinity through postdeposition treatments for large-scale applications but also restricts the development of hybrid materials. Thermotropic liquid crystals (LCs), especially nematic LCs, are known to favor the face-to-face slide past along the director of nematogens and can serve as liquid lubricants.[17−19] Investigations on LCs tuning the interface friction and controlling the droplet mobility have also been conducted.[20,21] However, the introduction of the lubricating phenomenon at the nanoscale and the underlying mechanism at the molecular level remain unexplored. Besides globally providing solvent vapor[22,23] or high pressure,[24] grafting mesogen-functionalized ligands on the surface of NCs could be a new pathway to promote the mobility of single NC building units on demand. The mobility of NCs can be observed during the reorganization of NCSL solids in experiments, and all atomistic (AA)[25−29] or coarse-grain (CG)[30−33] simulations can assist in comprehensively understanding the underlying ligand-mediated relative motions. These simulations are known to be capable of encapsulating the intricacies of the molecular features of surface ligands.[7,25,34,35]

In this study, we present the design of dendritic ligands end-functionalized with biphenyl mesogens. The ligands facilitate the reordering and reorientation of NCs in the substrate-

Received: September 28, 2023
Revised: December 20, 2023
Accepted: January 8, 2024
Published: January 31, 2024

deposited NCSLs as dry solids without any solvent assistance. We refer to this phenomenon as ligand lubrication, where the ligand shells prefer not to interdigitate. Reducing the interdigitation of the ligand chains may free up the NCs and unlock the local environment to grant better mobility.[36,37] A thermodynamically favored, close-packed NCSL with high crystallinity and preferred low-energy facets presented at a substrate is achieved through a topotactic transition from glassy state aggregates. The effectiveness of ligand design in manipulating the lubricating ability of ligands and consequently the movements of the NCs are demonstrated systematically. In parallel with experimental observations, CG molecular dynamics (MD) simulations elucidate that lubrication originates from the molecular interactions of ligands, where biphenyls form a shielding layer to prevent chain interdigitation. These new insights establish at a molecular level how ligand structure and interactions can affect the structural change and formation of NCSLs, thus providing a structure−property relationship of these stimuli-responsive nanomaterials on a multiscale level.

■ RESULTS AND DISCUSSION

The design of thermally triggerable lubricating ligands for dynamic NCSLs considers the following principles (Scheme 1). (1) Mesogenic: The mesogen functionalization should be added to the end of a ligand tail to introduce possible face-to-face sliding. (2) Stabilizing: The ligand shell should be capable of protecting the NCs at elevated temperatures. (3) Flexible: The ligand chains should have flexibility to avoid crystallizing on NCs and yield a high propensity for self-assembly.[37−39] Based on the first principle, biphenyl mesogens are introduced as tail groups (**L1**, **L2**, and **L3**). The fact that Au-**L1** fuses during heating shows the importance of the second principle (Figure S1). The dendritic structure, which is compact on the peripheral ligand chains and highly efficient in protecting NCs under thermal excursions,[40] serves as a skeleton on which to graft biphenyls (**L2** and **L3**). **L2** with alkyl chains and **L3** with triethylene glycol (TEG) chains are synthetically distinct in flexibility, leading to different responses to their NCSL structural changes, as shown in the following experiments. The corresponding nonpromesogenic ligands (**G1C12** and **G1TEG**) are also prepared as a comparison. All ligands are synthesized with atomic precision following our reported procedures.[41,42] It is the first time these designed ligands are used for dynamic NCSLs in a dried solid state comprising solely the ligand functionalized NCs. In the final NCSLs, the shell thickness is below 2 nm and surrounds an Au NC core of 5 nm in diameter, where the core occupies 20−27% of the volume in each building block (Table S2).[40,43]

Scheme 1. Library of Ligands and Their Schematic Models with Linear and Dendritic Structures, Including the Promesogenic Ligands (L1, L2, and L3), the Nonpromesogenic Ligands (G1C12 and G1TEG), and the Unfunctionalized Native Ligand (Oleylamine)[a]

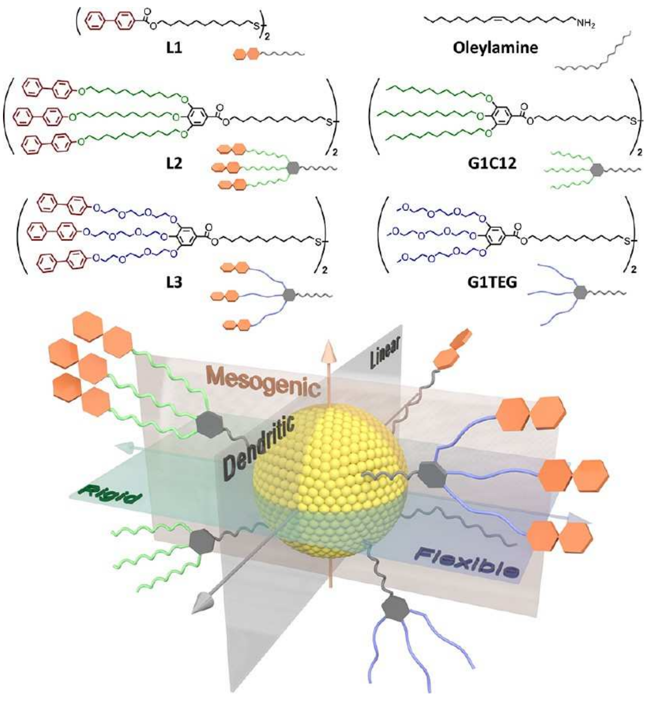

[a]The design principles of lubricating ligands being mesogenic, stabilizing, and flexible are shown as axes on the plot. The six ligands are placed based on their evaluation along each axis.

The evolution of the NCSL structures with each of the four dendritic ligands is monitored by *in situ* GISAXS during a heating−cooling cycle from 30 to 110 °C with a temperature interval of 20 °C and a thermal equilibration time of 20 min. The whole annealing process takes around 3 h. Au NCs are dropcast onto a Si substrate, dry under vacuum overnight, and form random aggregates. A face-centered cubic (FCC) or hexagonal close-packed (HCP) structure is formed directly from aggregates for NCs coated with promesogenic ligands after annealing. This confirms that the promesogenic ligands are actively assisting the NCs in assembling into the thermodynamically favored ordered structure from a disordered state instead of determining the final structure as a matrix or flux.[15,16] As a comparison, Au-**G1C12** and Au-**G1TEG** (Figure S2 and Tables S3 and S4) do not have a trend of increased order or orientational preference of NCSLs, confirming the role of biphenyl functionalization in lubrication.

Among all of the ligand systems in this study, **L3** with biphenyl mesogens, dendritic structures, and flexible TEG chains fulfills all three principles and yields the best lubricating ability (Figure 1). Initially, at 30 °C, the diffraction pattern exhibits a uniform ring with a broad peak, characteristic of poorly ordered aggregates (Figure 1a). From this diffraction ring, an oriented FCC pattern emerges as the temperature ramps from 30 to 110 °C. A small increase in interparticle distance, which is the distance between the centers of two neighboring NCs, from 7.95 to 8.21 nm is measured due to thermal expansion (Table S2). Distinct from previous studies,[8] the whole of the NCSL does not melt but crystallizes directly from the glassy state. The ordering of NCs improves continuously with extended heating, as evidenced by the narrowing of the diffraction peak width seen from GISAXS, and thus, increasing grain sizes are calculated from the Scherrer equation (Figure 1b and Table S3). This close-packed, thermodynamically favored structure remains after cooling. The NCSL crystallinity can be further improved by subjecting the sample to a subsequent annealing process to result in a single-crystal-like GISAXS pattern (Figure 1c).

Complementing the X-ray scattering data in the reciprocal space, transmission electron microscopy (TEM) images display the real-space topotactical structural change after annealing at 100 °C for 30 min, 1 h, and 4 h (Figure 1d).

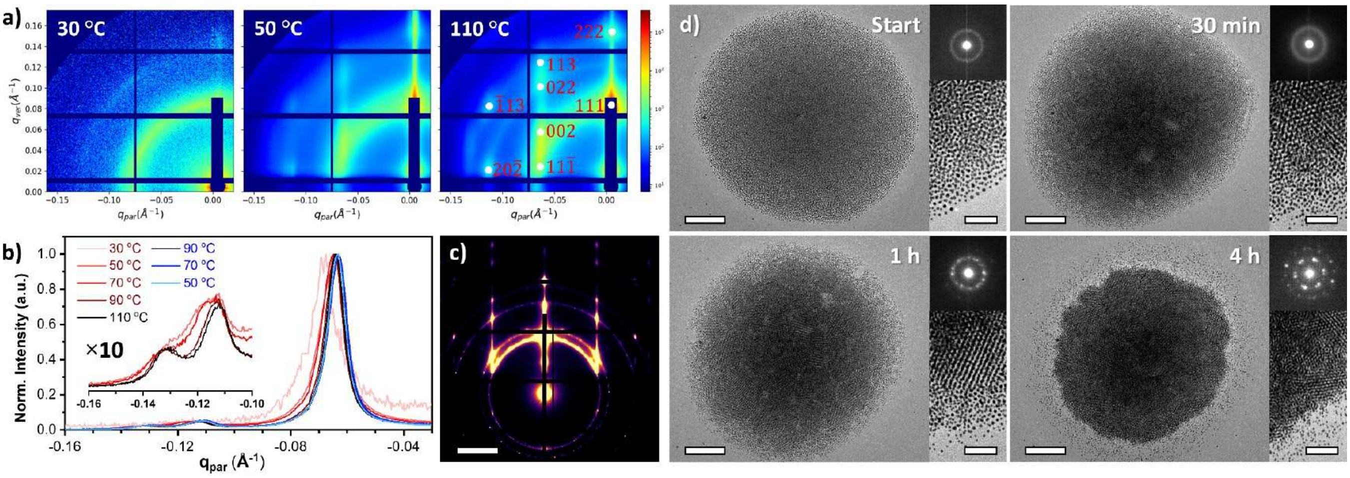

Figure 1. (a) Evolving of GISAXS of Au-**L3** drop-cast on an untreated Si substrate during heating. Peak indices are labeled. Negative q_{par} values represent the pattern on the left. (b) Horizontal line-cuts of the GISAXS images of Au-**L3** at q_{ver} = 0.03 Å^{-1}: heating from 30 to 110 °C and cooling from 110 to 50 °C; temperature interval, 20 °C. Resolving of the [311] and [220] peaks is shown in the inset (from 50 to 110 °C in heating). (c) GISAXS images of the FCC Au-**L3** film made after a subsequent annealing process. Scale bar: 0.05 Å^{-1}. (d) TEM images of the growth of Au-**L3** NCSLs over time. NCs are dropcast on a TEM grid and annealed at 100 °C for 30 min, 1 h, and 4 h. The upper insets are the corresponding selected-area SAED, and the lower insets are zoomed-in views of edge areas to show the migrating of NCs from edges. Scale bar: in the zoomed-out images, 200 nm; in the inset panels, 50 nm.

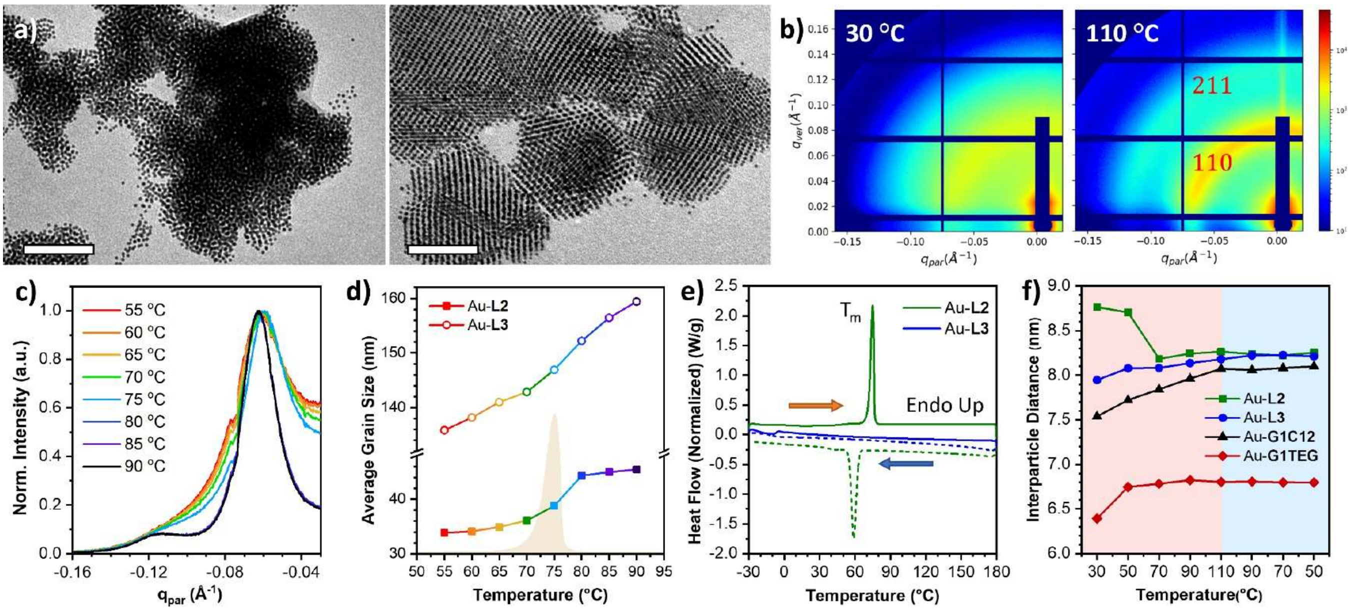

Figure 2. (a) TEM images of Au-**L2** drop-cast onto TEM grids at 25 °C (left) and preheated at 120 °C (right). Scale bar: 100 nm. (b) GISAXS of Au-**L2** dropcast on an untreated Si substrate at the beginning (30 °C) and at the maximum temperature (110 °C). The annealing process is the same as that in Figure 1a. Negative q_{par} values represent the pattern on the left. (c) Line-cuts of Au-**L2** with a finer temperature interval of 5 °C at q_{ver} = 0.03 Å^{-1}. (d) The average grain size of Au-**L2** and Au-**L3** was calculated from the deconvolution of the peak. The shaded area is a zoomed-in view of the Au-**L2** DSC melting peak. (e) DSC of the second heating−cooling cycle of Au-**L2** and Au-**L3**. Solid lines are heating curves, and dashed lines are cooling curves. (f) q values at different temperatures of Au-dendritic ligands in a full annealing cycle. The background is colored red for heating and blue for cooling. The relaxation of the expanded NCSLs might be slow.

The initial sample consists of mostly glassy state aggregates. More crystalline domains are seen with a longer annealing time, and a large-area ordered NCSL with a "jigsaw puzzle" morphology is formed eventually (Figure S5). The selected-area small-angle electron diffraction (SAED) shows the corresponding change in the polycrystalline NCSLs, matching well with the X-ray scattering data. Higher magnification images of the edge area indicate that the crystalline change starts from the center of the assembly with NCs at the edge migrating to form the ordered NCSLs. The statistics of the number of aggregates that contain at least one ordered domain at different annealing stages show an increase with time. The average area of crystalline domains also increases correspondingly (Figure S9). The individual character and narrow size distribution of Au-**L3** NCs remain after heating at 100 °C for 3 days (Figure S10), highlighting the use of dendritic structures to ensure thermal stability.

The alkyl chains in **L2** are less flexible than the TEG chains in **L3**. This molecular structural difference is reflected in the different thermal responses of Au-**L2** and Au-**L3** NCSLs. Au-

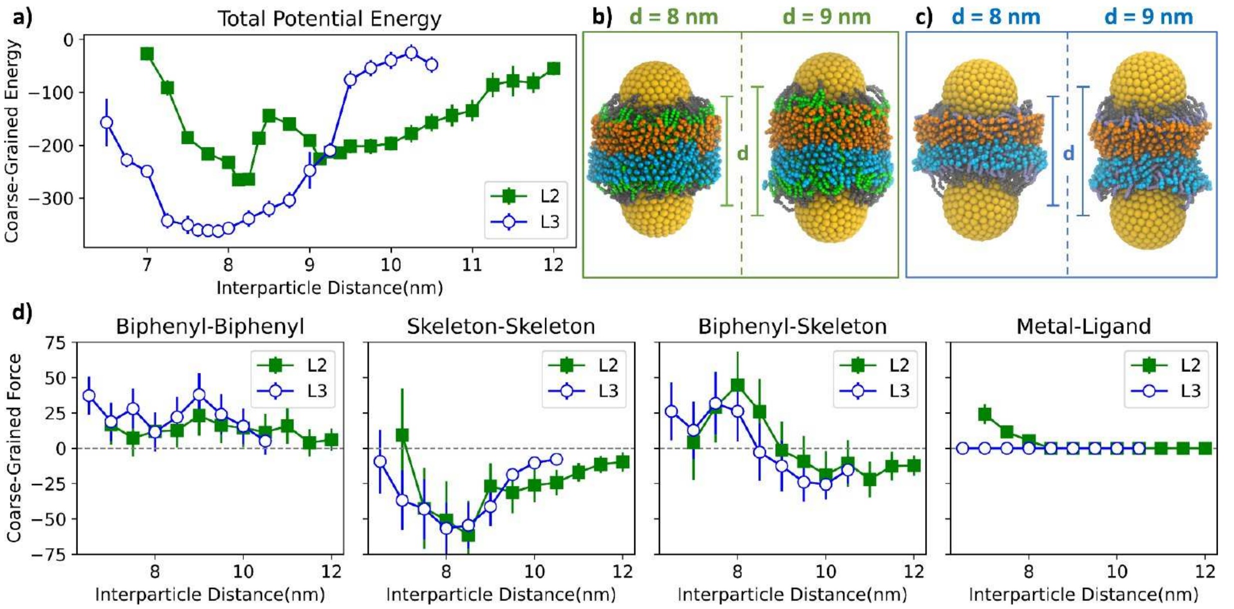

Figure 3. Dimer model of Au-**L2** and Au-**L3**. (a) Total energy of the simulated system when two NCs are confined to a series of given distances. Finer increments are taken around the minimum. The units are described in Figure S33. Ligand distributions for (b) Au-**L2** and (c) Au-**L3** dimer systems. Biphenyls on two NCs are colored separately in orange and blue. The color code is the same as in Scheme 1. Only half of the ligands on the shell of each particle are shown for clarity. (d) Force decomposition plots of Au-**L2** and Au-**L3** dimer systems. The force is first summed over the indicated groups on distinct particles and then projected along the center-to-center axis of the dimers. Interactions among biphenyls, skeleton, and NC core (metal) are analyzed separately. Positive forces indicate repulsion between NCs, and negative forces indicate attraction. Units of force are in (kcal/mol)/Å.

L2 NCs dropcast at room temperature mostly present random aggregations, and Au-**L2** dropcast at 120 °C can yield well-ordered, highly faceted NCSLs even with a faster solvent evaporation rate (Figure 2a), indicating **L2** can also alter the structure at elevated temperatures. However, no orientational preference is developed, as characterized by *in situ* GISAXS. Although the crystallinity of Au-**L2** does improve after the same annealing process as Au-**L3**, the final average grain size is 40 nm, whereas Au-**L3** has a grain size of 160 nm (Figure 2b, Table S3).

A finer temperature interval in annealing shows that Au-**L2** starts with a small narrowing in the peak width at low temperatures, presents a sharp shrink of peak widths and emergence of the secondary diffraction ring simultaneously at around 75 °C, and stays almost unchanged until 90 °C (Figure 2c). The crystallinity improvement of Au-**L2** displays a clear temperature threshold during annealing compared with the continuous change of Au-**L3** (Figure 2d, Figure S18). Differential scanning calorimetry (DSC) shows Au-**L2** assemblies have a sharp endothermic peak at 73 °C, matching the melting peak of the neat **L2** ligand and the turning temperature in Au-**L2** GISAXS. On the other hand, Au-**L3** only has a glass transition well below room temperature, reflecting the difference in the kinetics of NCSLs due to the flexibility of chains (Figure 2e and Figure S19).

In addition to the kinetic differences, near 70 °C, Au-**L2** also displays a thermal shrinking of the interparticle distance from 8.7 to 8.2 nm, echoing the transition associated with the DSC endothermic peak (Figure 2e), while the other three dendritic ligands all show a normal thermal expansion during heating (Figure 2f and Figure S8). It is therefore inferred that the ligand interdigitation is developed with the melting of the whole ligand shell or even just the tails, allowing adjacent NC cores to get closer and causing a macroscopic thermal shrinking.[27]

A microscopic simulation investigation is carried out to unravel two things: (1) how the ligand molecular structures affect the ligand interdigitation and (2) how the ligand structure and interdigitation affect the ordering of NCs. Simulating these systems presents a significant challenge: The size and geometry of the NC cores with their ligands must be considered, making the cost to employ AA simulations[25,26] or *ab initio* simulations notably high.[34,44−46] Conversely, simplified geometric representations of the NCs and their ligand shells as spheres or polyhedrons[47,48] may not fully recover the crucial interactions of the promesogenic ligands. These requirements underscore the significance of utilizing intermediate-resolution, coarse-grain (CG) models to investigate nanoscale features of ligand-functionalized NC cores and the associated molecular-level conformational properties.

We developed a CG model to tackle this challenge. We adopt parameters from the prototype of our ligands, biphenyl-based LCs, which have been proven capable of capturing fundamental aggregation properties previously.[49,50] To simulate the TEG chains, new representations of the ether moieties and their associated potential terms are parametrized (Figures S28 and S29). Rigid spherical metal shells of diameter 5.1 nm represent the NC cores, and ligands are uniformly attached to mimic the experimental grafting density[41] (Table S1, Figure S27). Each ligand is a set of spherical "beads" representing phenyls, oxygens, and carbons. A description of parametrization and modeling is presented in the simulation section of the Supporting Information.

A dimer model consisting of two NCs and their respective ligand shells has been constructed to investigate the interaction between neighboring NCs at varying interparticle distances.[51,52] Generally, the dimer simulation considers a range of

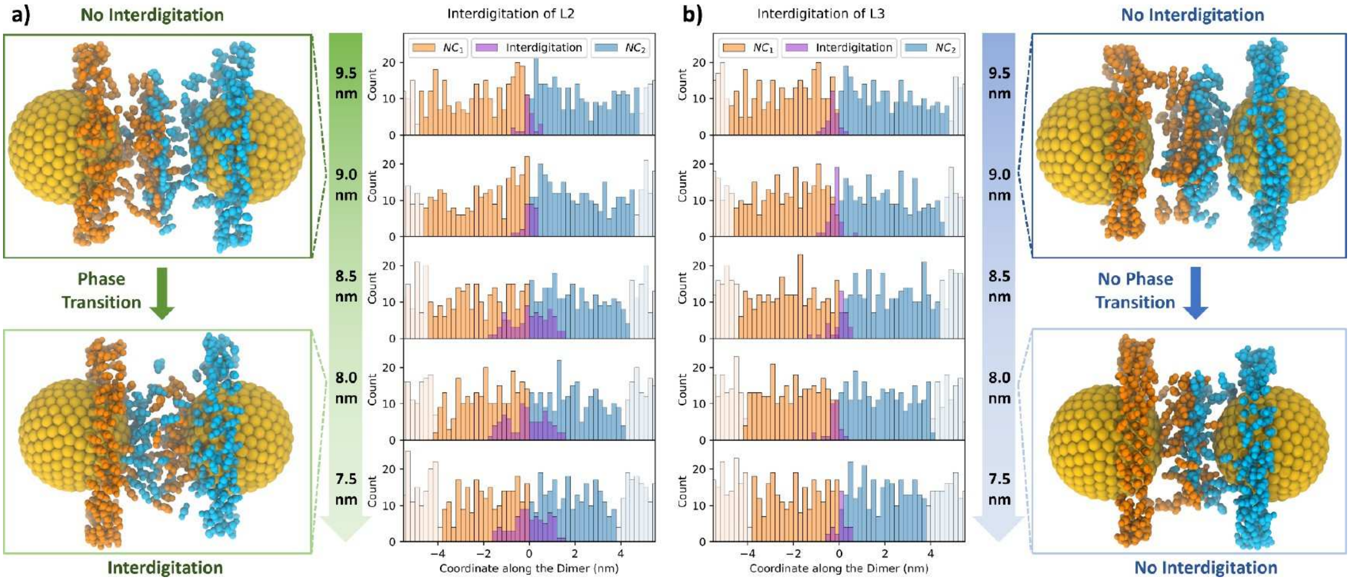

Figure 4. Ligand interdigitation on two NC cores at different interparticle distances. (a) Au-**L2** before (9.0 nm) and after (8.0 nm) the phase transition. Biphenyls are orange on the first NC and blue on the second NC. Only biphenyls on the interacting hemispheres are shown for clarity. The distribution probability diagrams of the ligand shells at interparticle center-to-center distances of 9.5, 9.0, 8.5, 8.0, and 7.5 nm, respectively, are shown on the right. Areas in orange and blue are ligand distributions on the interacting hemispheres. The overlapping area of the two distributions (purple) represents the extent of ligand interdigitation. Shadowed areas show a part of the distribution on the opposite hemisphere of the ligand shell for each NC. (b) Au-**L3** dimer at an interparticle distance of 9.0 nm (top) and 8.0 nm (bottom). The distribution probability diagrams of the ligand shell at different interparticle distances are shown on the left.

distances that are comparable to experiments for both Au-**L2** (7.0−12.0 nm) and Au-**L3** (6.5−10.5 nm). The calculations suggest that the potential curve of Au-**L2** is different from that of Au-**L3**. While the latter contains a single minimum at 7.75 nm (similar to 8.0 nm in experiments), the former shows a lower energy minimum at 8.25 nm and an additional broad minimum in the range of 9−10 nm (Figure 3a). These two minima of the Au-**L2** curve are a result of the **L2** ligands transitioning from one stable configuration to another more stable one as the cores get closer. In the following discussion, we show these two configurations are noninterdigitated and interdigitated ligand shells. The existence of a barrier suggests the requirement of an activation energy to reduce the interparticle distance. This is consistent with the endothermic, freedom-increasing process manifested in experiments as the melting of **L2** at around 75 °C (Figures 2e and S8). Since the minimum at 8.25 nm is lower in energy, the dimer changes from the broad minimum between 9 and 10 nm to the closer interparticle distance, corresponding to the thermal shrinking observed in experiments (Figure 2e). Snapshots of Au-**L2** and Au-**L3** at 8 and 9 nm display the ligand configuration (Figure 3b,c); the Au-**L2** ligand corona appears to be cylindrically shaped, while that of Au-**L3** shows more narrowing at the contact interface. The apparent difference is consistent with the difference in flexibility of the ligands.

Further analysis through force decomposition considers the ligand biphenyl and the skeleton that comprises all remaining atoms in **L2** or **L3** (Figure S35). Force contributions to the net force between the NCs from different segments of the ligands are elucidated (Figure 3d and Figure S38). First, for all distances, the bulky biphenyl−biphenyl groups mainly show repulsion and the skeleton−skeleton interactions mainly show attraction (Figure 3d). The skeleton−skeleton attraction thus appears to be the driving force for particle adhesion. Second, the biphenyl−skeleton interaction varies from attractive to repulsive as the distance between the two particles decreases (Figure 3a). This repulsive force is higher in Au-**L2** than in Au-**L3**. Around the first energy minimum of Au-**L2** (Figure 3a), there is a sudden drop of the skeleton−skeleton force and an increase of the biphenyl−skeleton repulsion, which indicates a decrease of the relative distance between these groups. Third, a weak repulsion between one NC metal and ligands on the other NC is observed when the distance is less than 8 nm for Au-**L2**; this metal−ligand repulsive interaction, denoting a reduction in the distance between one NC core and the ligands originating from the adjacent NC, is consistent with the ligand interdigitation. Conversely, the core−ligand force is zero for all distances with Au-**L3** (Figure 3d), suggesting that there is little ligand interpenetration.

For this dimer model, the spatial distribution of ligands is different in Au-**L2** and Au-**L3** (Figure 4). The findings confirm a noticeable difference in the amount of interdigitation of **L2** and **L3** in the dimer simulations. Limited overlap of the two biphenyl distributions, one associated with each particle, occurs at longer separations in the dimer of Au-**L2** (Figure 4a). However, when the interparticle distance is smaller than 8.5 nm, a significant overlap of the **L2** distribution is observed, showing that an increasing number of biphenyls have invaded the adjacent NC ligand shell (Figure 4a). The enhanced level of interdigitation is the new configuration of the ligand shells, which provides a stronger skeleton-skeleton interaction and stabilizes a new minimum. In contrast, Au-**L3** shows little overlap of the biphenyl distributions for the same set of interparticle distances, indicating little interdigitation of the ligand layers (Figure 4b). Notably, the lack of interdigitation has also been reported previously with other ligand systems.[36] It is also noteworthy that the nonpromesogenic ligands (those without biphenyl) in this study exhibit a high level of interdigitation even at a long distance of 9.0 nm (Figure

S40), which is consistent with the previous understanding of alkyl and polymeric ligands.[27,53,54]

From the dimer model, the flexible biphenyl functionalized TEG chains prevent entangling and result in a non-interdigitated interparticle region. On the other hand, the less flexible alkyl chains in **L2** provide multiple stable conformations, as reflected in the interparticle distance observed experimentally. The most stable conformation has ligand interdigitation (Figure 3a), effectively preventing the particles from reorientating. However, in the dimer model, it is possible to underestimate the interdigitation of **L3** ligands because of this low coordination environment. Higher coordination consistent with high-density lattices must be considered to better understand Au-**L3** NCSLs.

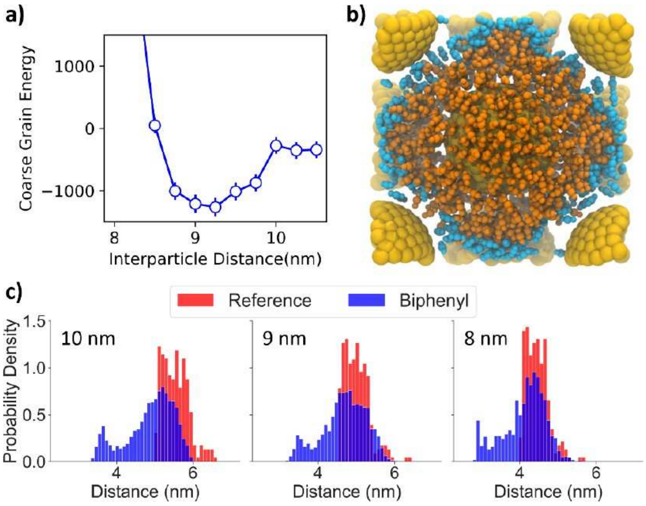

Figure 5. Simulation of Au-**L3** NCs in an FCC unit cell. (a) Total energy of the system when the unit cell is defined at a series of given interparticle distances. (b) Simulated **L3** ligand shell at a minimum energy (9.0 nm interparticle distance). Biphenyls from the central NC are colored orange, and biphenyls from the surrounding NCs are blue. (c) Simulated distributions (blue) of distance from the NC center to the biphenyl in the FCC unit cell at interparticle distances between 8 and 11 nm. Sampled reference distributions of distances from the NC center to the surface of the corresponding Wigner−Seitz unit cell (red) are used for comparison. The results for Au-**L2** in the FCC unit cell can be found in the Supporting Information.

We build an FCC unit cell with one particle at the center of the cube. The simulation for a series of unit cell lengths shows that the optimum interparticle distance falls around 9 nm, more than 1 nm larger than the minimum in the dimer model (Figure 5a). Notably, at this optimum distance, the ligand shell is confined in the Wigner−Seitz cell (Figure 5b). The boundary between the ligand shell of the central NC and the surrounding NCs is distinct, with biphenyls forming a shield. Minimal interdigitation is observed, as confirmed by the statistics of the relative positions of biphenyls. The distance of biphenyls from the central particle is calculated, and the distribution is compared with a theoretical distribution of distances to the Wigner-Seitz cell surface (reference) at the given interparticle distance (Figure 5c). The biphenyl distribution coincides with that of the reference distribution for large distances with infrequent instances of exceeding the boundary. This demonstrates that essentially all biphenyls remain in the Wigner−Seitz cell at low (10.0 nm) and optimum (9.0 nm) interparticle distances; even at a high density (8.0 nm), few biphenyls penetrate the Wigner−Seitz cell. This simulation of Au-**L3** FCC NCSLs confirms that the interdigitation level of **L3** is indeed lower than that of **L2** (Figure S44), and the boundary between NCSLs is therefore well-defined. The decreased entanglement in Au-**L3** facilitates sliding between outer shells and grants each NC better mobility. With thermal stimuli, the enhanced mobility of Au-**L3** relative to Au-**L2** is expected to allow the NCSLs to reorder into a thermodynamically favored close-packed structure.

A time- and temperature-resolved kinetic study of Au-**L3** NCSLs with a different thickness sheds light on the sequence-prioritized, bottom-up reordering mechanism of the origin of the NCSL orientation preference (Figure 6a and Figure S11). The Au-**L3** NCSLs can undergo a seemingly endless reordering like topotaxy,[55] until well-ordered while being maintained at a certain elevated temperature. Temperatures only change the rate of reordering. The lubricating of the interparticle region frees up the local binding of NCs and the thermal energy gives the NCs mobility to move to close-packed configurations. The crystallinity of NCSLs develops almost simultaneously at different depths of the NCSL film as GISAXS from different incident angles displays the FCC pattern at the same time. In contrast, the orientation develops gradually from the bottom to the top. When the NCSLs in the bulk region have already formed a well-oriented pattern (0.15° incidence), the NCSLs on the surface still show a partially emphasized polycrystalline pattern (0.05° incidence), indicating a chronological sequence in forming the orientation at different depths. Indeed, a higher density of NCs and the interface of substrates make the NCs at the bottom region easier to realize the favored orientation. This lubricating mechanism differs significantly from solvent-vapor annealing,[22,23] even though both methods may yield similar structural outcomes.

A thick Au-**L3** film is prepared by dropcasting a doubled amount of NCs on a same-size substrate (compared to the film in Figure 1) to slow down the process. Consistent with Figure 1b, at 30 °C, the uniform diffraction ring shows glassy state aggregates without long-range order (Figure 6b). As the temperature increases, the (111) spot emerges at 65 °C after 20 min, while the $(11\bar{1})$ spot evolves more slowly and appears together with the higher-ordered diffraction rings when the temperature reaches 70 °C after another 10 min. These sharp higher-order diffraction rings indicate the formation of long-range-ordered FCC NCSLs. Different narrowing rates of the (111) and $(11\bar{1})$ peaks show quantitively the anisotropic growth of the SLs (Figure 6c). This observation suggests that the out-of-plane order develops faster than the in-plane order, which may also be promoted by the substrate.

The orientation development can be quantitatively understood by defining a factor from the evolution of the (022) and (113) peaks (in-plane packing) compared to the (111) peak (out-of-plane packing) (Figure 6d and Figures S15 and S16). While samples with three thicknesses all show a similar rate of forming oriented NCSLs in the bulk (0.15°), the thinnest sample is the fastest to be oriented at the top surface (0.05°). Therefore, the orientation should develop gradually from the bottom, where (111) facets are presented at the substrate interface, toward the top. When annealing at a fixed temperature of 50 °C, the rate of NCSL formation is slower in the thick sample compared to the medium and thin samples. However, the final crystallinity of the thick sample can surpass that of the other two samples (Figure 6e). Together with the

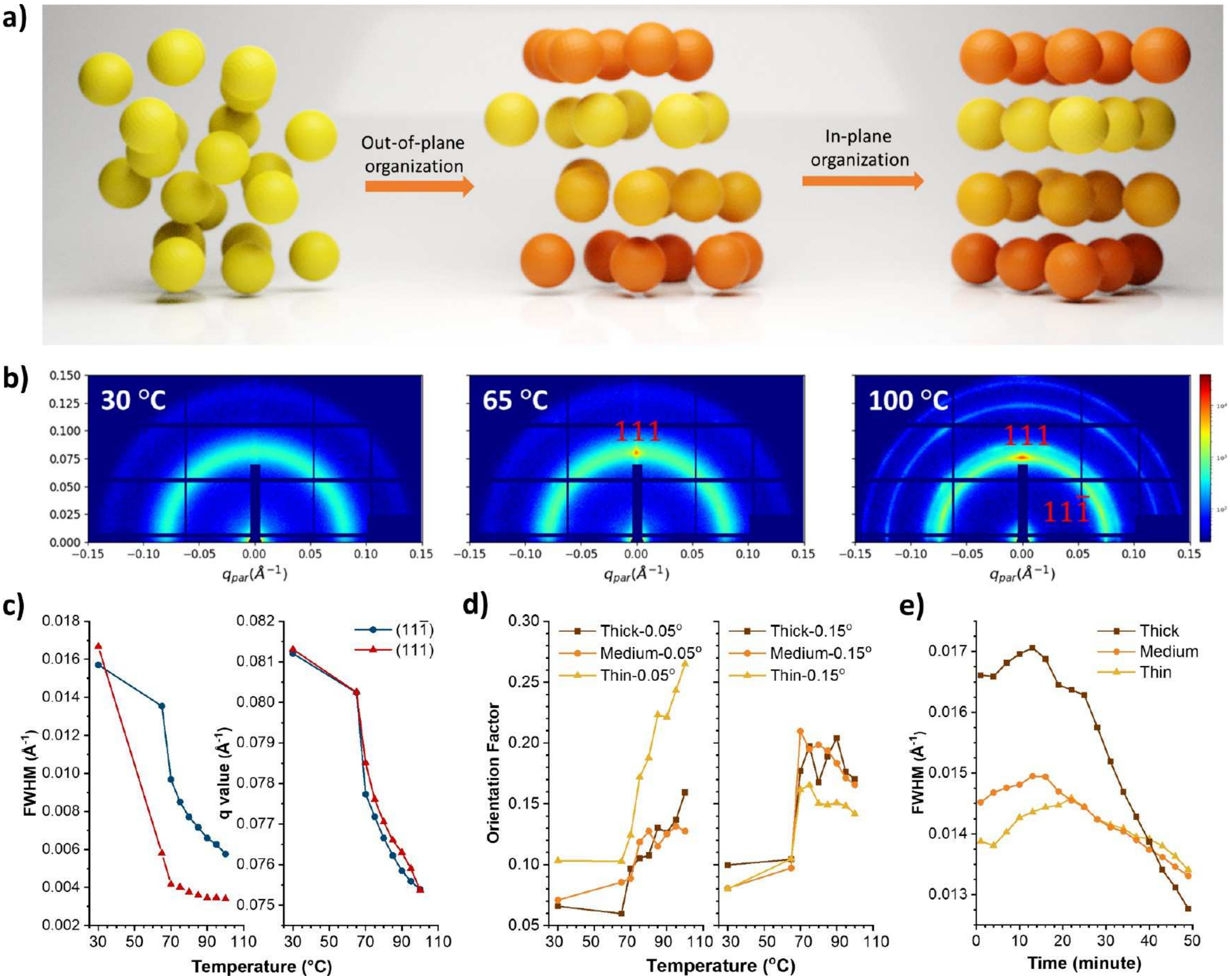

Figure 6. (a) Illustration showing the reorganization process of Au-**L3** NCSLs on the substrate. (b) *In situ* GISAXS patterns for the thick Au-**L3** NCSLs at 30 °C, 65 °C, and 100 °C during heating. (c) Peak width (left) and q (right) extracted from the line-cut of the q-images at 0.05° incident angle. Out-of-plane (111) peaks are from the vertical line-cut at $q_{\text{par}} = 0$ Å^{-1}. In-plane (11$\bar{1}$) peaks are from a horizontal line-cut at $q_{\text{ver}} = 0.0265$ Å^{-1}. (d) Formation rate of in-plane orientation factored by the intensity ratio of (022)/(111) peaks of Au-**L3** samples with a different thickness during thermal annealing at 0.05° (left) and 0.15° (right) incident angle. (e) Deconvoluted peak widths of the out-of-plane (111) peak corresponding to time of Au-**L3** at 50 °C.

chronological reordering and reorientation of these FCC NCSLs, it can be seen the structural change starts from the interface between NCSLs and substrates where the most thermodynamically stable (111) facets are preferred to form and then propagates throughout the whole NCSLs with the assistance of the noninterdigitated, lubricating **L3** ligand shell revealed by simulation.

We reiterate the design principles; the ligands should terminate with mesogens, stabilize the NCs across a range of temperatures, and exhibit sufficient flexibility to allow reconfiguration and self-assembly. The nonpromesogenic ligands in this study both have a high level of ligand interdigitation, and no lubricating phenomenon can be observed. When all three principles are achieved, the ligand lubrication phenomenon of **L3** can increase crystallinity and improve the orientational preference of NCSLs simultaneously. **L2** fulfills two of the three principles, with biphenyls and the dendritic structure in the present study but without the TEG chains to increase flexibility. The biphenyls for **L2** are insufficient to shield the interdigitation of ligands and result in limited reordering before transitioning to the interdigitated status. However, the phase transition of the **L2** ligands can introduce a lattice densification of NCSLs.

The densification phenomenon of Au-**L2** showed great potential in laser writing applications. As a demonstration, a laser beam passes swiftly through an Au-**L2** film at a wavelength close to the plasmonic distinction peak of Au NCs (Figure S25), a mark of the annealed region with a width of 2 μm shows up under optical microscopy due to plasmonic heating (Figure 7a and Figure S20). Compared to the unilluminated areas on both sides, the laser-treated region has a smoother surface like that of a thermally annealed sample, confirmed by atomic force microscopy (AFM) with a 4-fold decrease in roughness (Figures 7b,e and S21). The thickness of the treated region decreases due to the densification of Au-**L2** NCSLs with lattice shrinking. TEM images show the individual Au-**L2** NCs do not degrade or fuse upon illumination and the NCSLs become better crystallized

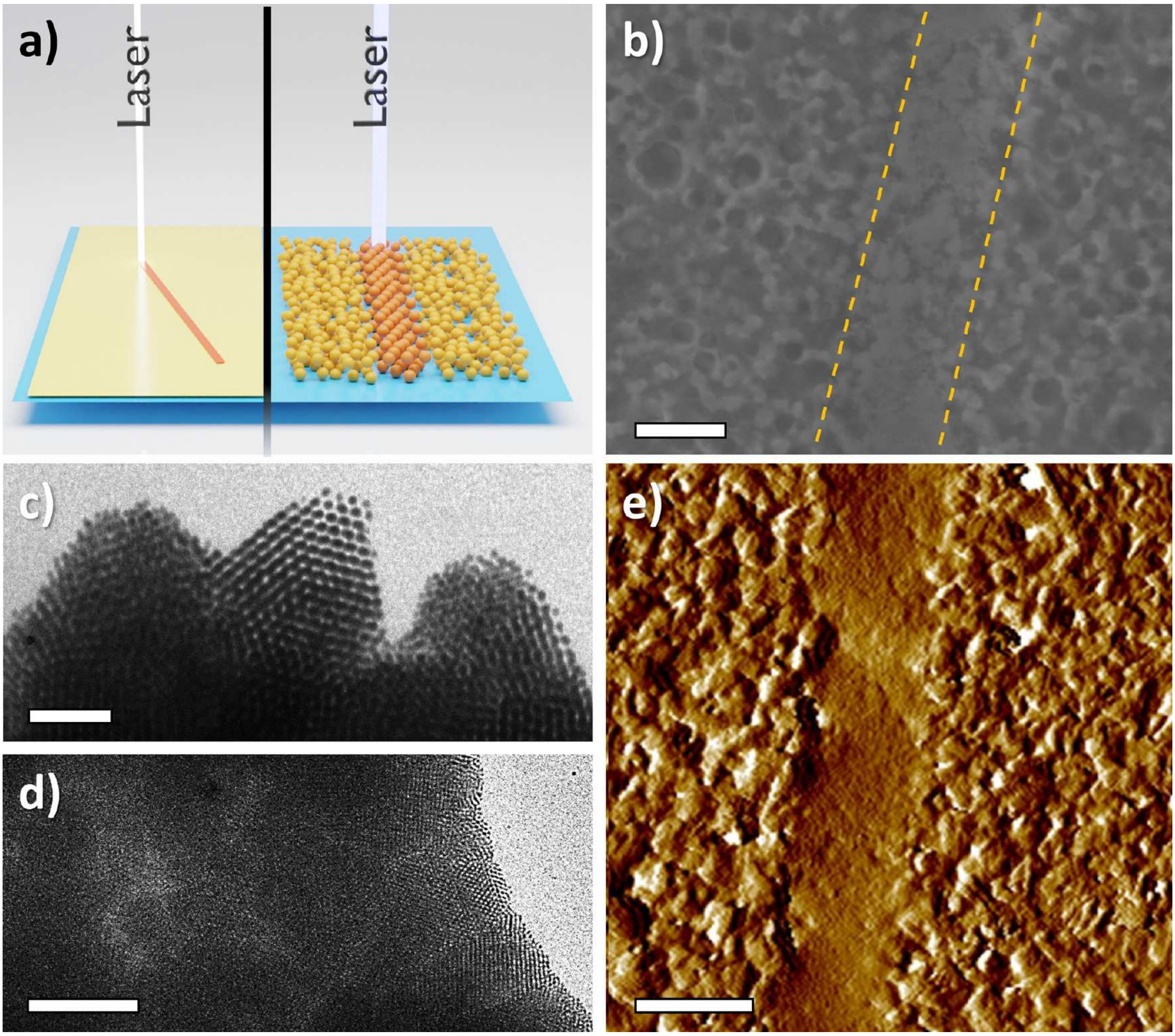

Figure 7. (a) Left: Illustration of using a laser to anneal the Au-**L2** film. Right: Schematics of the annealed area with an ordered structure. (b) SEM image of a laser-annealed area, highlighted by a dashed line. Scale bar: 1 μm. (c, d) TEM images of the laser-annealed area in (b). Scale bars: (c) 50 and (d) 200 nm. (e) Surface profile of the same area in (b) with AFM after laser annealing. Scale bar: 2 μm.

(Figure 7, c, and d), matching well with the result of thermally heating the substrate. Applying the laser illumination to the Au-**L3** film could also trigger structural changes, but the annealed region is not as trackable as Au-**L2** due to the absence of film densification, the limitation of the laser beam size, and the resolution of optical microscopy. The annealed NCSL films from either thermal annealing or laser treatment show no red-shift of plasmonic extinction, again proving the NCs do not fuse (Figure S25). The conductivity of the Au-**L2** thin film increases by 3 orders of magnitude after thermal annealing, possibly due to ligand interdigitation and better ordering in the NCSLs. However, it is still limited as an insulator with a face-to-face distance of 3 nm[56] (Table S5). The absence of red-shifts of plasmonic extinctions also matches with the insulating result and no observed fusing of NCs.

■ CONCLUSION

We show that designing and introducing thermally responsive, dendritic promesogenic ligands on the surface of colloidal NCs create a lubrication phenomenon. The integration of biphenyls at the ligand tails effectively prevents the entangling of chains, as unveiled by simulations. This lubrication of interparticle spaces provides the NCs with the ability to move, leading to the reorganization and reorientation of the NCSLs. This insight highlights the distinction between lubrication in dry solid systems and other scenarios involving solvents or matrix support, introducing a new dimension to manipulate the mobility of NC building blocks within NCSLs. The design principles for lubricating ligands are formulated with broad applicability by systematically comparing ligands with varying molecular structures by using theoretical and experimental analyses. The implications of these findings extend to diverse fields such as plasmonics and optoelectronics, where material properties are profoundly influenced by ordering and interparticle spacing. Additionally, the straightforward post-processing setup and high spatial control employed in this approach will greatly facilitate the production of NCSLs on scales ranging from meso- to bulk-level.

■ ASSOCIATED CONTENT

Supporting Information

The Supporting Information is available free of charge at https://pubs.acs.org/doi/10.1021/jacs.3c10706.

Simulation video of Au-**L3** FCC superlattices (MP4)

Experimental details, additional experimental and simulation data, figures, and supplementary discussion (PDF)

■ AUTHOR INFORMATION

Corresponding Authors

Jeffery G. Saven − *Department of Chemistry, University of Pennsylvania, Philadelphia, Pennsylvania 19104, United States;* orcid.org/0000-0001-5027-7241; Email: saven@sas.upenn.edu

Christopher B. Murray − *Department of Chemistry and Department of Materials Science and Engineering, University of Pennsylvania, Philadelphia, Pennsylvania 19104, United States*; Email: cbmurray@sas.upenn.edu

Authors

Yifan Ning − *Department of Chemistry, University of Pennsylvania, Philadelphia, Pennsylvania 19104, United States;* orcid.org/0000-0001-8033-0904

Shengsong Yang − *Department of Chemistry, University of Pennsylvania, Philadelphia, Pennsylvania 19104, United States;* orcid.org/0000-0002-1386-7549

Dai-Bei Yang − *Department of Chemistry, University of Pennsylvania, Philadelphia, Pennsylvania 19104, United States*

Yi-Yu Cai − *Department of Electrical and Systems Engineering, University of Pennsylvania, Philadelphia, Pennsylvania 19104, United States*

Jun Xu − *Department of Electrical and Systems Engineering, University of Pennsylvania, Philadelphia, Pennsylvania 19104, United States*

Ruipeng Li − *National Synchrotron Light Source II, Brookhaven National Laboratories, Upton, New York 11973, United States*

Yugang Zhang − *Center for Functional Nanomaterials, Brookhaven National Laboratories, Upton, New York 11973, United States*

Cherie R. Kagan − *Department of Chemistry, Department of Materials Science and Engineering, and Department of Electrical and Systems Engineering, University of Pennsylvania, Philadelphia, Pennsylvania 19104, United States;* orcid.org/0000-0001-6540-2009

Complete contact information is available at: https://pubs.acs.org/10.1021/jacs.3c10706

Author Contributions

[#]Y.N., S.Y., and D-B.Y. contributed equally to this work.

Notes

The authors declare no competing financial interest.

■ ACKNOWLEDGMENTS

The authors acknowledge primary support from NSF STC-IMOD under Award DMR2019444 and partial characterization support from the Office of Naval Research Multidisciplinary University Research Initiative (MURI) Award ONR N00014-18-1-2497. Y.N. acknowledges the support from NSF University of Pennsylvania Materials Research Science and Engineering Center (MRSEC) under Award DMR-1720530 for ligand synthesis. D-B.Y. acknowledges a John G. Miller Fellowship from the University of Pennsylvania. J.X. acknowledges the support from NSF Engineering Research Center for Internet of Things for Precision Agriculture (Grant NSF-1941529). J.G.S. acknowledges support from DOE (Grant DE-SC0019282). C.B.M. also acknowledges the Richard Perry University Professorship at the University of Pennsylvania. This research used resources of the Center for Functional Nanomaterials and the CMS beamline (11-BM) of the National Synchrotron Light Source II, both supported by the U.S. DOE Office of Science Facilities at Brookhaven National Laboratory under Contract DE-SC0012704. We thank Dr. H. Zhang for the discussions and help at the beamline. This work was carried out in part at the Singh Center for Nanotechnology, which is supported by the NSF National Nanotechnology Coordinated Infrastructure Program under Grant NNCI-2025608. We thank Dr. Y. Morimitsu, Dr. G. Doerk, and Dr. S. Cetindag for their help with the thermal analysis. We thank Dr. T. Zhang for his help with modeling and parametrizing. Simulations and modeling were performed using allocation TG-CHE110041 from the Advanced Cyberinfrastructure Coordination Ecosystem: Services & Support (ACCESS) program, which is supported by National Science Foundation Grants 1548562, 2138259, 2138286, 2138307, 2137603, and 2138296.

■ REFERENCES

(1) Zornberg, L. Z.; Lewis, D. J.; Mertiri, A.; Hueckel, T.; Carter, D. J. D.; Macfarlane, R. J. Self-Assembling Systems for Optical Out-of-Plane Coupling Devices. *ACS Nano* **2023**, *17* (4), 3394−3400.

(2) Kang, Y.; Ye, X.; Chen, J.; Cai, Y.; Diaz, R. E.; Adzic, R. R.; Stach, E. A.; Murray, C. B. Design of Pt-Pd Binary Superlattices Exploiting Shape Effects and Synergistic Effects for Oxygen Reduction Reactions. *J. Am. Chem. Soc.* **2013**, *135* (1), 42−45.

(3) Nie, Z.; Petukhova, A.; Kumacheva, E. Properties and Emerging Applications of Self-Assembled Structures Made from Inorganic Nanoparticles. *Nat. Nanotechnol.* **2010**, *5* (1), 15−25.

(4) Cherniukh, I.; Rainò, G.; Stöferle, T.; Burian, M.; Travesset, A.; Naumenko, D.; Amenitsch, H.; Erni, R.; Mahrt, R. F.; Bodnarchuk, M. I.; Kovalenko, M. V. Perovskite-Type Superlattices from Lead Halide Perovskite Nanocubes. *Nature* **2021**, *593* (7860), 535−542.

(5) Zhao, Q.; Gouget, G.; Guo, J.; Yang, S.; Zhao, T.; Straus, D. B.; Qian, C.; Oh, N.; Wang, H.; Murray, C. B.; Kagan, C. R. Enhanced Carrier Transport in Strongly Coupled, Epitaxially Fused CdSe Nanocrystal Solids. *Nano Lett.* **2021**, *21* (7), 3318−3324.

(6) Lee, M. S.; Yee, D. W.; Ye, M.; Macfarlane, R. J. Nanoparticle Assembly as a Materials Development Tool. *J. Am. Chem. Soc.* **2022**, *144*, 3330.

(7) Boles, M. A.; Engel, M.; Talapin, D. V. Self-Assembly of Colloidal Nanocrystals: From Intricate Structures to Functional Materials. *Chem. Rev.* **2016**, *116* (18), 11220−11289.

(8) Lewandowski, W.; Fruhnert, M.; Mieczkowski, J.; Rockstuhl, C.; Górecka, E. Dynamically Self-Assembled Silver Nanoparticles as a Thermally Tunable Metamaterial. *Nat. Commun.* **2015**, *6* (1), 6590.

(9) Macfarlane, R. J.; Lee, B.; Jones, M. R.; Harris, N.; Schatz, G. C.; Mirkin, C. A. Nanoparticle Superlattice Engineering with DNA. *Science* **2011**, *334*, 204−208.

(10) Nykypanchuk, D.; Maye, M. M.; van der Lelie, D.; Gang, O. DNA-Guided Crystallization of Colloidal Nanoparticles. *Nature* **2008**, *451* (7178), 549−552.

(11) Lee, S.; Calcaterra, H. A.; Lee, S.; Hadibrata, W.; Lee, B.; Oh, E.; Aydin, K.; Glotzer, S. C.; Mirkin, C. A. Shape Memory in Self-Adapting Colloidal Crystals. *Nature* **2022**, *610* (7933), 674−679.

(12) Zhang, Y.; Pal, S.; Srinivasan, B.; Vo, T.; Kumar, S.; Gang, O. Selective Transformations between Nanoparticle Superlattices via the Reprogramming of DNA-Mediated Interactions. *Nat. Mater.* **2015**, *14* (8), 840−847.

(13) Li, Z.; Fan, Q.; Yin, Y. Colloidal Self-Assembly Approaches to Smart Nanostructured Materials. *Chem. Rev.* **2022**, *122* (5), 4976−5067.

(14) Gliozzi, A. S.; Miniaci, M.; Chiappone, A.; Bergamini, A.; Morin, B.; Descrovi, E. Tunable Photo-Responsive Elastic Metamaterials. *Nat. Commun.* **2020**, *11* (1), 2576.

(15) Zhao, Y.; Thorkelsson, K.; Mastroianni, A. J.; Schilling, T.; Luther, J. M.; Rancatore, B. J.; Matsunaga, K.; Jinnai, H.; Wu, Y.; Poulsen, D.; Fréchet, J. M. J.; Paul Alivisatos, A.; Xu, T. Small-Molecule-Directed Nanoparticle Assembly towards Stimuli-Responsive Nanocomposites. *Nat. Mater.* **2009**, *8* (12), 979−985.

(16) Lewandowski, W.; Jatczak, K.; Pociecha, D.; Mieczkowski, J. Control of Gold Nanoparticle Superlattice Properties via Mesogenic Ligand Architecture. *Langmuir* **2013**, *29* (10), 3404−3410.

(17) Fischer, T. E.; Bhattacharya, S.; Salher, R.; Lauer, J. L.; Ahn, Y.-J. Lubrication by a Smectic Liquid Crystal. *Tribol. Trans.* **1988**, *31* (4), 442−448.

(18) Carrión, F.-J.; Martínez-Nicolás, G.; Iglesias, P.; Sanes, J.; Bermúdez, M.-D. Liquid Crystals in Tribology. *Int. J. Mol. Sci.* **2009**, *10* (9), 4102−4115.

(19) Usol'tseva, N. V.; Smirnova, A. I. Liquid Crystals as Lubricants. *Lubricants* **2019**, *7* (12), 111.

(20) Borbora, A.; Xu, Y.; Dey, S.; Wang, X.; Yao, Y.; Mandal, B. B.; Wang, X.; Manna, U. Lubricated Interfaces Enabling Simultaneous Pulsatile and Continuous Chemical Release Modes. *Adv. Mater.* **2023**, *35* (31), 2302264.

(21) Xu, Y.; Rather, A. M.; Yao, Y.; Fang, J.-C.; Mamtani, R. S.; Bennett, R. K. A.; Atta, R. G.; Adera, S.; Tkalec, U.; Wang, X. Liquid Crystal-Based Open Surface Microfluidics Manipulate Liquid Mobility and Chemical Composition on Demand. *Sci. Adv.* **2021**, *7* (40), No. eabi7607.

(22) Wang, Y.; Chen, J.; Zhu, C.; Zhu, B.; Jeong, S.; Yi, Y.; Liu, Y.; Fiadorwu, J.; He, P.; Ye, X. Kinetically Controlled Self-Assembly of Binary Polymer-Grafted Nanocrystals into Ordered Superstructures via Solvent Vapor Annealing. *Nano Lett.* **2021**, *21* (12), 5053−5059.

(23) Hanrath, T.; Choi, J. J.; Smilgies, D.-M. Structure/Processing Relationships of Highly Ordered Lead Salt Nanocrystal Superlattices. *ACS Nano* **2009**, *3* (10), 2975−2988.

(24) Bai, F.; Bian, K.; Huang, X.; Wang, Z.; Fan, H. Pressure Induced Nanoparticle Phase Behavior, Property, and Applications. *Chem. Rev.* **2019**, *119* (12), 7673−7717.

(25) Li, B.; Bian, K.; Lane, J. M. D.; Salerno, K. M.; Grest, G. S.; Ao, T.; Hickman, R.; Wise, J.; Wang, Z.; Fan, H. Superfast Assembly and Synthesis of Gold Nanostructures Using Nanosecond Low-Temperature Compression via Magnetic Pulsed Power. *Nat. Commun.* **2017**, *8* (1), 14778.

(26) Cosseddu, S.; Pascazio, R.; Giansante, C.; Manna, L.; Infante, I. Ligand Dynamics on the Surface of CdSe Nanocrystals. *Nanoscale* **2023**, *15* (16), 7410−7419.

(27) Kaushik, A. P.; Clancy, P. Explicit All-Atom Modeling of Realistically Sized Ligand-Capped Nanocrystals. *J. Chem. Phys.* **2012**, *136* (11), 114702.

(28) Srivastava, I.; Peters, B. L.; Lane, J. M. D.; Fan, H.; Salerno, K. M.; Grest, G. S. Mechanics of Gold Nanoparticle Superlattices at High Hydrostatic Pressures. *J. Phys. Chem. C* **2019**, *123* (28), 17530−17538.

(29) Winslow, S. W.; Tisdale, W. A.; Swan, J. W. Prediction of PbS Nanocrystal Superlattice Structure with Large-Scale Patchy Particle Simulations. *J. Phys. Chem. C* **2022**, *126* (33), 14264−14274.

(30) Mitra, G.; Chang, C.; McMullen, A.; Puchall, D.; Brujic, J.; Hocky, G. M. A Coarse-Grained Simulation Model for Colloidal Self-Assembly *via* Explicit Mobile Binders. *Soft Matter* **2023**, *19* (23), 4223−4236.

(31) Ilnytskyi, J. M.; Slyusarchuk, A.; Saphiannikova, M. Photocontrollable Self-Assembly of Azobenzene-Decorated Nanoparticles in Bulk: Computer Simulation Study. *Macromolecules* **2016**, *49* (23), 9272−9282.

(32) Zhu, H.; Fan, Z.; Song, S.; Eggert, D.; Liu, Y.; Shi, W.; Yuan, Y.; Kim, K.-S.; Grünwald, M.; Chen, O. Dual Atomic Coherence in the Self-Assembly of Patchy Heterostructural Nanocrystals. *ACS Nano* **2022**, *16* (9), 15053−15062.

(33) Zhang, Z.; Glotzer, S. C. Self-Assembly of Patchy Particles. *Nano Lett.* **2004**, *4* (8), 1407−1413.

(34) Ye, X.; Chen, J.; Engel, M.; Millan, J. A.; Li, W.; Qi, L.; Xing, G.; Collins, J. E.; Kagan, C. R.; Li, J.; Glotzer, S. C.; Murray, C. B. Competition of Shape and Interaction Patchiness for Self-Assembling Nanoplates. *Nat. Chem.* **2013**, *5* (6), 466−473.

(35) Winslow, S. W.; Swan, J. W.; Tisdale, W. A. The Importance of Unbound Ligand in Nanocrystal Superlattice Formation. *J. Am. Chem. Soc.* **2020**, *142* (21), 9675−9685.

(36) Geva, N.; Shepherd, J. J.; Nienhaus, L.; Bawendi, M. G.; Van Voorhis, T. Morphology of Passivating Organic Ligands around a Nanocrystal. *J. Phys. Chem. C* **2018**, *122* (45), 26267−26274.

(37) Li, C.; Liu, L.; Zhang, Z.; Zhang, D.; Yi, S.; Yang, H.; Fan, Z. Anisotropy in Near-Spherical Colloidal Nanoparticles. *ACS Nano* **2023**, *17*, 17873.

(38) Yang, Y.; Qin, H.; Jiang, M.; Lin, L.; Fu, T.; Dai, X.; Zhang, Z.; Niu, Y.; Cao, H.; Jin, Y.; Zhao, F.; Peng, X. Entropic Ligands for Nanocrystals: From Unexpected Solution Properties to Outstanding Processability. *Nano Lett.* **2016**, *16* (4), 2133−2138.

(39) Love, J. C.; Estroff, L. A.; Kriebel, J. K.; Nuzzo, R. G.; Whitesides, G. M. Self-Assembled Monolayers of Thiolates on Metals as a Form of Nanotechnology. *Chem. Rev.* **2005**, *105* (4), 1103−1169.

(40) Diroll, B. T.; Jishkariani, D.; Cargnello, M.; Murray, C. B.; Donnio, B. Polycatenar Ligand Control of the Synthesis and Self-Assembly of Colloidal Nanocrystals. *J. Am. Chem. Soc.* **2016**, *138* (33), 10508−10515.

(41) Ning, Y.; Liu, Z.; Yang, S.; Morimitsu, Y.; Osuji, C. O.; Murray, C. B. Design of Dendritic Promesogenic Ligands for Liquid Crystal-Nanoparticle Hybrid Systems. *Chem. Mater.* **2023**, *35* (9), 3532−3544.

(42) Elbert, K. C.; Jishkariani, D.; Wu, Y.; Lee, J. D.; Donnio, B.; Murray, C. B. Design, Self-Assembly, and Switchable Wettability in Hydrophobic, Hydrophilic, and Janus Dendritic Ligand-Gold Nanoparticle Hybrid Materials. *Chem. Mater.* **2017**, *29* (20), 8737−8746.

(43) Diroll, B. T.; Weigandt, K. M.; Jishkariani, D.; Cargnello, M.; Murphy, R. J.; Hough, L. A.; Murray, C. B.; Donnio, B. Quantifying "Softness" of Organic Coatings on Gold Nanoparticles Using Correlated Small-Angle X-Ray and Neutron Scattering. *Nano Lett.* **2015**, *15* (12), 8008−8012.

(44) Zasada, F.; Piskorz, W.; Cristol, S.; Paul, J.-F.; Kotarba, A.; Sojka, Z. Periodic Density Functional Theory and Atomistic Thermodynamic Studies of Cobalt Spinel Nanocrystals in Wet Environment: Molecular Interpretation of Water Adsorption Equilibria. *J. Phys. Chem. C* **2010**, *114* (50), 22245−22253.

(45) Holmberg, N.; Chen, J.-C.; Foster, A. S.; Laasonen, K. Dissolution of NaCl Nanocrystals: An Ab Initio Molecular Dynamics Study. *Phys. Chem. Chem. Phys.* **2014**, *16* (33), 17437−17446.

(46) Zherebetskyy, D.; Scheele, M.; Zhang, Y.; Bronstein, N.; Thompson, C.; Britt, D.; Salmeron, M.; Alivisatos, P.; Wang, L.-W. Hydroxylation of the Surface of PbS Nanocrystals Passivated with Oleic Acid. *Science* **2014**, *344* (6190), 1380−1384.

(47) Anderson, J. A.; Glaser, J.; Glotzer, S. C. HOOMD-Blue: A Python Package for High-Performance Molecular Dynamics and Hard Particle Monte Carlo Simulations. *Comput. Mater. Sci.* **2020**, *173*, 109363.

(48) Yang, S.; LaCour, R. A.; Cai, Y.-Y.; Xu, J.; Rosen, D. J.; Zhang, Y.; Kagan, C. R.; Glotzer, S. C.; Murray, C. B. Self-Assembly of

Atomically Aligned Nanoparticle Superlattices from Pt-Fe3O4 Heterodimer Nanoparticles. *J. Am. Chem. Soc.* **2023**, *145* (11), 6280−6288.

(49) Zhang, J.; Su, J.; Ma, Y.; Guo, H. Coarse-Grained Molecular Dynamics Simulations of the Phase Behavior of the 4-Cyano-4′-Pentylbiphenyl Liquid Crystal System. *J. Phys. Chem. B* **2012**, *116* (7), 2075−2089.

(50) Zhang, J.; Guo, H. Transferability of Coarse-Grained Force Field for nCB Liquid Crystal Systems. *J. Phys. Chem. B* **2014**, *118* (17), 4647−4660.

(51) Gupta, U.; Escobedo, F. A. Ligand Interactions and Nanoparticle Shapes Guide the Pathways toward Interfacial Self-Assembly. *Langmuir* **2022**, *38* (5), 1738−1747.

(52) Schapotschnikow, P.; Pool, R.; Vlugt, T. J. H. Molecular Simulations of Interacting Nanocrystals. *Nano Lett.* **2008**, *8* (9), 2930−2934.

(53) Wang, Z.; Christodoulides, A. D.; Dai, L.; Zhou, Y.; Dai, R.; Xu, Y.; Nian, Q.; Wang, J.; Malen, J. A.; Wang, R. Y. Nanocrystal Ordering Enhances Thermal Transport and Mechanics in Single-Domain Colloidal Nanocrystal Superlattices. *Nano Lett.* **2022**, *22* (12), 4669−4676.

(54) Plunkett, A.; Kampferbeck, M.; Bor, B.; Sazama, U.; Krekeler, T.; Bekaert, L.; Noei, H.; Giuntini, D.; Fröba, M.; Stierle, A.; Weller, H.; Vossmeyer, T.; Schneider, G. A.; Domènech, B. Strengthening Engineered Nanocrystal Three-Dimensional Superlattices via Ligand Conformation and Reactivity. *ACS Nano* **2022**, *16* (8), 11692−11707.

(55) Abelson, A.; Qian, C.; Salk, T.; Luan, Z.; Fu, K.; Zheng, J.-G.; Wardini, J. L.; Law, M. Collective Topo-Epitaxy in the Self-Assembly of a 3D Quantum Dot Superlattice. *Nat. Mater.* **2020**, *19* (1), 49−55.

(56) Chen, W.; Guo, J.; Zhao, Q.; Gopalan, P.; Fafarman, A. T.; Keller, A.; Zhang, M.; Wu, Y.; Murray, C. B.; Kagan, C. R. Designing Strong Optical Absorbers *via* Continuous Tuning of Interparticle Interaction in Colloidal Gold Nanocrystal Assemblies. *ACS Nano* **2019**, *13* (7), 7493−7501.